# Fabrication of high-conductivity RGO film at a temperature lower than 1500 °C by electrical current

Meijuan Lv[1,2], Qinwei Wei[1,2], Shuo Cao[1,2], Jingdong Guo[1,2,*] (iD), Wencai Ren[1,2], and Huiming Cheng[1,2]

[1] Institute of Metal Research, Chinese Academy of Sciences, Shenyang 110016, China
[2] School of Materials Science and Engineering, University of Science and Technology of China, Shenyang 110016, China

## ABSTRACT

Fabricating conductive graphene films by assembling graphene oxide (GO) sheets is highly desired for many applications, however a very high temperature around 3000 K is usually required to repair the $sp^2$ structure for traditional thermal annealing. Here, an electric field assisted Joule heating method was developed to repair the $sp^2$ structure in GO at a temperature lower than 1500 °C. The resulting free-standing graphene film shows a high electrical conductivity (~ 1840 S/cm) and high C/O ratio (132), both of which are much higher than those of thermally reduced GO films under the same temperature. These findings provide new possibilities for fabricating high-quality graphene films in an energy-efficient and low-cost manner.

## 1 Introduction

Graphene has received more and more attention in electronics and energy devices for its ultrahigh electrical conductivity, lightweight, and excellent mechanical performance [1–7]. So far, a lot of work has been done in the preparation of graphene, but limited success has been achieved in the preparation of high-quality macro and thick graphene films. Graphene oxide reduction method is widely accepted in microelectronic field for its low-cost and large-scale production. In recent years, a variety of reduction methods of graphene oxide have been employed to assemble heat/electricity-conducting film in microelectronic field, mainly divided into chemical

reduction and thermal reduction according to the reduction mechanism [8, 9]. Chemical reduction usually achieved at lower temperature (< 150 °C), but impurities are inevitably introduced in the reduction process, resulting in poor conductivity of the film. Thermal reduction method has the advantage of high purity, but to obtain high-quality film, it often needs to reach the graphitization temperature as high as above 3000 K and a long-time reduction process, resulting in a waste of resources and time. Therefore, an efficient and energy-saving method to produce excellent electricity/heating properties graphene is imperative.

Lately, a new method named joule heating method [10–14] was brought up to reduce graphene oxide. Hu's [10] group developed a stable 3000 K joule

heating method to produce the reduced GO (RGO) film with less defects/impurities and larger graphitic sp2 domains, which enables its record-high conductivity and mobility of 6300S/cm and 320 cm$^2$ V$^{-1}$ s$^{-1}$ at room temperature. Gao et al. [13] applied joule heating to effectively reduce GO at an ultra-high temperature ($\sim$ 2750 K) in a short time, leading to highly crystalline graphene structure and freestanding RGO film with high dc conductivity of 3112 S/cm. Sang Ouk Kim's group [14] presented electrothermal reduction (Joule heating) to restore the sp$^2$ domain of GO fibers and achieved a high electrical conductivity of 1020 S/cm. Although the joule heating method achieved high conductivity in the RGO film, it is also accompanied by high temperature up to 3000 K, which limits its application.

Although the effect of electric current on graphene is rarely reported, the research on applying electric current to metal is fruitful [15–18]. According to the results in metallic materials, electric current can effectively accelerate the atomic diffusion, phase transformation, dissolution, chemical reaction, and so on. Inspired by these results, we believe that it may be able to reduce GO film at a lower temperature by electric current.

In this work, we developed an electric field assisted reduction (electro-reduction) method to reduced GO film under a much lower temperature ($<$ 1500 °C) than those reported previously ($\sim$ 3000 K). The resulting RGO film shows a high electrical conductivity of $\sim$ 1840 S/cm and a C/O ratio of 132, both of which are much higher than those of thermally reduced GO films under the same temperature. These findings open new possibilities for better reducing GO and further utilizing it in electronic and energy storage devices.

## 2 Experimental

### 2.1 Materials

All following reagents were used as received: A GO dispersion was prepared by improved Hummer's method [19]. GO films were obtained by scanning centrifugal casting method [20, 21]. Analytical-grade reagents ferrous sulfate ($FeSO_4 \cdot 7H_2O$), cobalt chloride ($CoCl_2 \cdot 6H_2O$), polyethylene glycol (PEG-400), hydrazine ($N_2H_4 \cdot H_2O$) and cyclohexane ($C_6H_{12}$) were used for preparing magnetic particle.

### 2.2 Reduction of GO film with direct current and furnace

The GO film was thermally pre-reduced at 500 °C for 1 h in an argon-filled tube furnace with the heating rate of 1 °C/min. The aim of pre-reduction is to reduce the huge resistance of GO films due to the presence of the oxygen-contained groups and trigger the electro-reduction. The pre-reduced GO film (Pre-RGO) is sandwiched between two pieces of quartz glass and fix with a stainless-steel clip, with both ends bonds to copper tapes. The reduction experiment was conducted by applying direct current (dc) to the film in a quartz tube full of argon, as illustrated in Fig. 1. The current applied on the samples is 10A, corresponding to current density $5 \times 10^7$ A/m$^2$, and the reduction time was set as 1 min, 10 min, 1 h and 8 h. The temperature of the samples was detected by an infrared thermometer (E3MH-F2-L-0-0) and recorded by the digital collector (HIOKI LR8401-21). In order to verdict the non-thermal effect in the electro-reduction process, thermal reduction was performed at the same temperature as the electro-reduction process. Due to the temperature change during the electro-reduction process (caused by the resistance change of sample), the temperature at 1 h during the electro-reduction process was selected as the reference temperature for the thermal reduction (Fig. 2). The detail parameters of the electro-reduction are shown in Table S1.
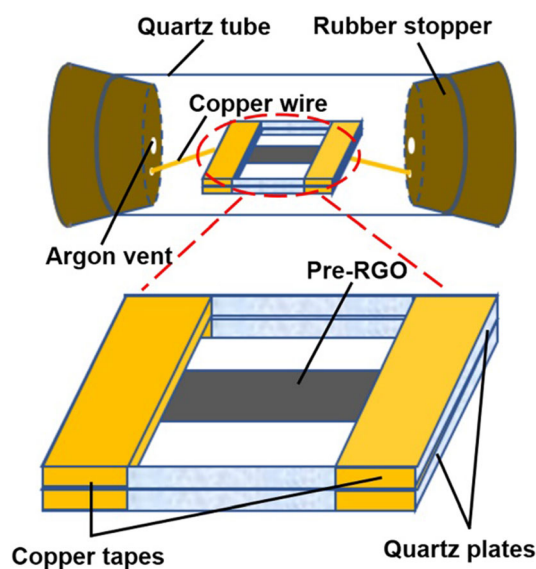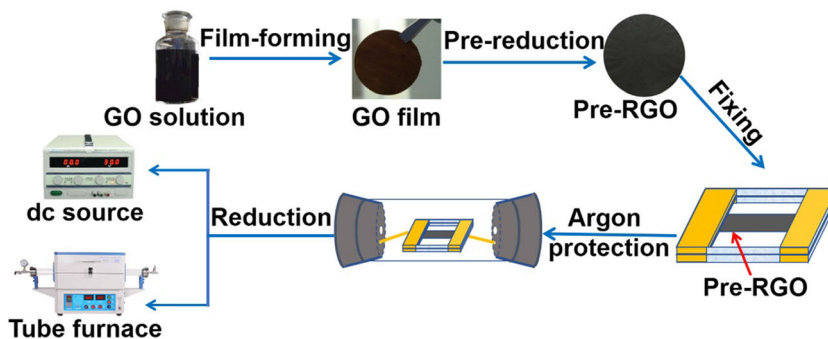


**Fig. 1** Schematic diagram of the experimental device

**Fig. 2** Flow chart of the whole reduction process



## 2.3 Characterization

Morphology structures of GO, RGO film and magnetic particles were characterized using field emission-scanning electron microscope (SEM, FEI Quanta 600/SUPRA 55). Transmission electron microscopes (TEM, FEI Tecnai F30/JEOL JEM-2100) were used to characterize the degree of crystallization. Raman spectra were collected on a WITec alpha300R with laser excitation wavelength of 532 nm. X-ray diffraction (XRD, Cu Ka radiation, D8 Advance, BRUKER/AXS, Germany), X-ray photoelectron spectroscopy (XPS, PHI Quanta SXM) were applied to elements analysis. The electric conductivity of the reduced film was measured by a four-electrode method (RTS-9).

## 3 Results and discussion

The temperature profile of the samples under electric current was recorded, as shown in Fig. 3. Insets are optical images of the sample at different times. When an electric current was applied to the sample, the temperature of the sample first rises rapidly due to the joule heat. When the temperature reaches equilibrium, the resistance of the graphene film decreases due to the electro-reduction, the temperature of the sample gradually reduced. As time continue increases, the temperature curve turns to flat, and then rises. This phenomenon may be caused by the reaction [22] between quartzes and the graphene film (Fig S1), which caused defects on the surfaces of RGO films and the increase in resistance.

$$SiO_2 + C = SiC + CO \qquad (1)$$

In order to eliminate the influence of the reaction between graphene and quartz glass, the top layer of the sample was removed before the following characterization.
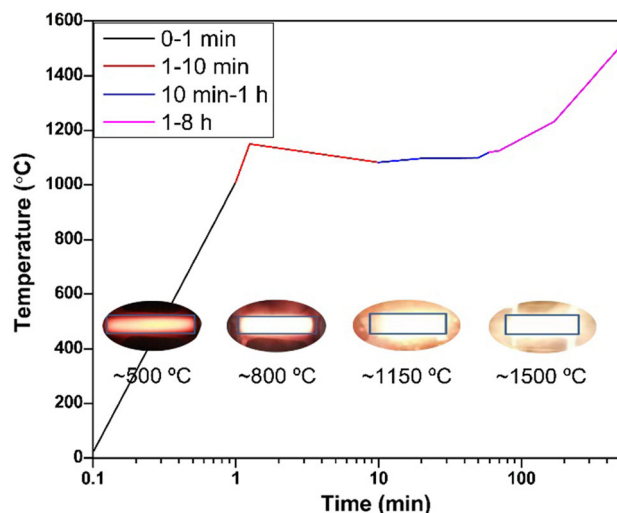


**Fig. 3** Time versus temperature curve of the RGO film reduced at 10 A. Insets show the optical images of the RGO film during electro-reduction

The surface morphology and cross-sectional SEM images of the Pre-RGO sample and electro-reduced sample are shown in Fig. 4a–d. It can be seen that a lot of wrinkles, which were formed due to the overlap of adjacent flakes during the film forming process, were observed on the surface of Pre-RGO samples. Whereas after electro-reduction under 10A for 1 h, the wrinkles on the surface of the film have almost disappeared, as shown in Fig. 4b. The electro-reduced sample has a much smooth surface and a more compact stack than the Pre-RGO sample. As we know, the overlap of adjacent flakes not only reduce the compactness of the Pre-RGO film, but also hinder the transport of the carrier (mainly electrons), making the wrinkles regions have larger electric resistance. During the electro-reduction, these areas will generate more joule heat, resulting in higher temperature, so the overlapping flakes will be welded into larger flakes. As a result, the wrinkles in the sample became

**Fig. 4** SEM images of Pre-reduced sample and electro-reduced sample. Surface morphology of **a** Pre-reduced sample and **b** electro-reduced sample (10 A, 1 h); Cross-section SEM images of **c** Pre-RGO film and **d** electro-reduced sample (10 A, 1 h)
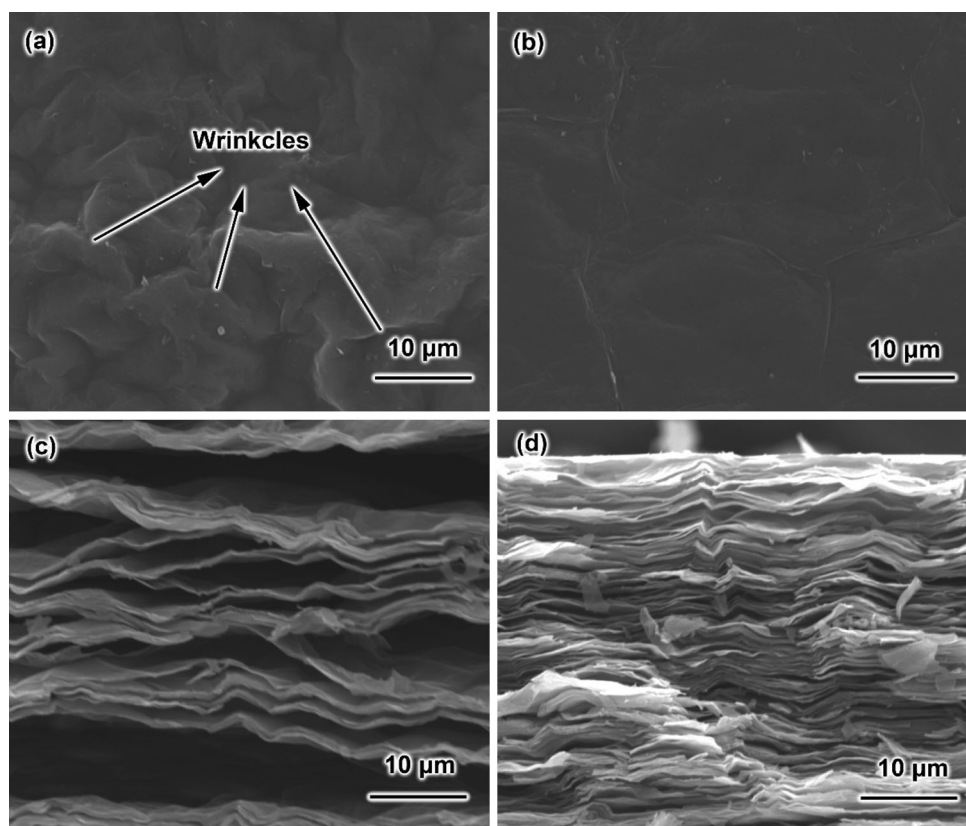


less and flatter after electro-reduction (Fig. 4b), which is beneficial for the compactness of the film, as shown in Fig. 4c and d. Figures 5a and b are high resolution TEM (HRTEM) images of the Pre-RGO sample and electro-reduced sample. The insets are their selected area electron diffraction (SAED) patterns. The TEM morphology of the Pre-RGO sample is disordered, and its SAED shows a ring pattern corresponding to the amorphous microstructure, which may be attributed to the presence of a varieties of oxygen-containing functional groups in it, which leads to a very high defect ratio. After electro-reduction, the sample shows crystal stripes in HRTEM. The distance between two stripes is ~ 0.21 nm, close to the lattice spacing of graphene. The diffraction pattern shows of it also indicates the high crystallization in the sample after electro-reduction.

XRD patterns of the Pre-RGO sample and electro-reduced (10 A-reduction) sample are shown in Fig. 5c. The Pre-RGO sample shows a (0 0 2) characteristic peak at 24.1° with a full width at half maximum (FWHM) of 2.46°, while for the electro-reduced sample, the (0 0 2) peak shifts to 26.09° and becomes much narrower with a FWHM of 0.80°.

According to Brag's law, the interlayer distance (d-spacing) of the Pre-RGO sample and electro-reduced sample is 0.3673 nm and 0.3397 nm, respectively. The smaller d-spacing indicates that the oxygen-containing functional groups were removed, and the narrower and sharper characteristic peak indicate that a more ordered structures and larger graphite domain size, which is consistent with the results of SEM and TEM.

XPS spectra denote the composition of the fabricated RGO films. As shown in Fig. 6a, the ratio of C/O increased from the original 3.79 (GO film: O% atom = 20.86%) to 132.33 (10A-reduced RGO film: O% atom = 0.75%), an increase of 35 times, which confirms that the electro-reduction has removed the oxygen-containing functional groups effectively. By comparing the C 1s fine scan of the Pre-RGO film, the 1150 °C-thermal reduced film and the 10A-electro-reduction film, the deoxidization is further discussed. After reduction, the C–C/C=C (sp$^2$ carbon) peak at 284.6 eV increased while the C–O (~ 286.3 eV), C=O (~ 287.8 eV) and COOH (~ 289 eV) [8, 23–25] decreased in the both reduction method. After electro-reduction, the C=O and COOH disappeared and
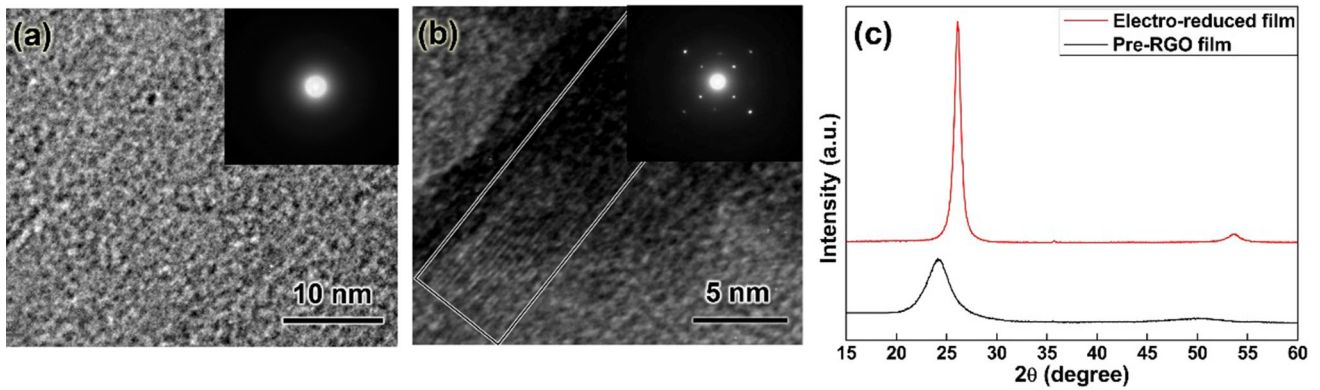
**Fig. 5** TEM images of samples before (**a**) and (**b**) after electro-reduction. **c** XRD patterns of samples of before and after electro-reduction. Insets of **a** and **b** show the diffraction patterns of (**a**) and (**b**)
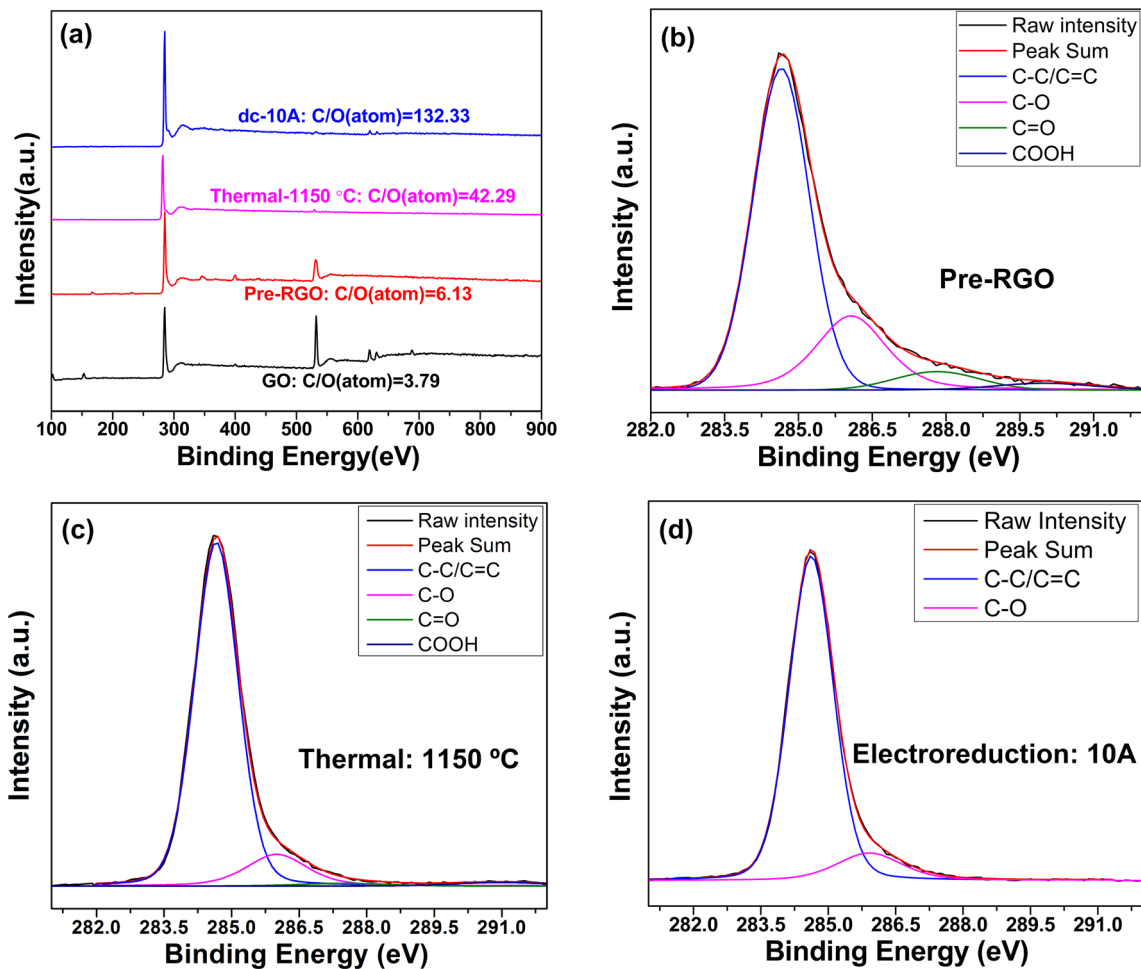


**Fig. 6** XPS analysis. **a** XPS element survey scan of GO, Pre-RGO, thermal reduction (1150 °C, 1 h) and electro-reduction (10 A, 1 h), respectively (top to bottom); Element fine scan: **b** C1s of Pre-RGO film, **c** thermal reduced RGO film (1150 °C, 1 h) and **d** electro-reduced film (10 A, 1 h)

showed a more symmetric C peak compare with that of thermal reduction. The content of oxygen-containing functional groups of the reduced RGO films by the two method are denoted in the Table.1. Apparently, apart from C–C/C=C, content of various oxygen-containing functional groups in electro-

reduced sample were all less than those in thermal reduced sample, which indicated that electro-reduction works more efficiently.

Raman spectra of the Pre-RGO sample, electro-reduced (10A-reduction) samples and thermal reduced sample (1150 °C, 1 h) are shown in Fig. 7. Note that the D, G and 2D characteristic band were shown at $\sim$ 1360, 1635 and 2675 cm$^{-1}$ of the curve, and they are related to defect-induced breathing mode, the stretching mode of the C–C bonds and the degree of crystallization in the graphene-like structure, respectively [26, 27]. The D to G band intensity ratio ($I_D/I_G$) is used to judge the proportion of defects in the RGO films. Compare with the Raman spectrum of the Pre-RGO, the G bands and 2D band of the electro-reduced films are sharper (Fig. 7a). It indicates the increase of sp2 domain size and crystallization, which is contributed to the effective electro-reduction. In addition, it is shown in Fig. 8b that the $I_D/I_G$ first increased and then decreased with the electro-reduction time. The $I_D/I_G$ changed from 0.854 of Pre-RGO to 0.99 of the electro-reduced film for 1 min, and then decreases to 0.16 when the reduction time is 8 h.

In order to clarify the effect of electric current on the repair of the sp$^2$ structure in GO, nano FeCo magnetic particle loading test was carried out on the reduced samples to characterize the defects on the RGO film. The FeCo nano particles were synthesized by using a modified chemistry technique (More details about fabricating FeCo on RGO films are shown in supplementary information) [28]. Figure 8a shows the morphology of Pre-RGO film loaded with nano FeCo magnetic particle. The surface is relatively smooth, and FeCo aggregates are mainly distribute in the wrinkle position. For the RGO film electro-reduced for 1 min, the FeCo aggregates loaded on the surface were more numerous, almost a quarter of the surface was covered by them, as show in Fig. 8b. For the RGO films reduced for 10 min, 1 h and 8 h, as the reduction times increased, FeCo aggregates loaded on the surface gradually decreased, and the

distribution of them are more and more uniform, as shown in the result of image processing (Table S2) performed on Fig. 8c–e. In addition, the size of the aggregates was characterized by an image analysis software, and they are also getting smaller (Fig. S2).

It is believed that the size and the distribution of the magnetic particle aggregates are inextricably linked to the defects. In order to understand their relationship, density functional theory (DFT) calculations were performed to investigate the nucleation process of the magnetic particles on electro-reduced RGO films with a monovacancy and 5–8–5 defect (divacancy), respectively (More details are in supplementary information). The nucleation process of the FeCo particle on RGO films is simulated by Cambridge Serial Total Energy Package (CASTEP). The modules are shown in Fig. 9. The driving force (the nucleation energy ($E_N$) is represented by the difference of chemical potential ($\Delta\mu$):

$$E_N = \Delta\mu = E_{RGO/FeCo} - E_{RGO} - E_{FeCo} \qquad (2)$$

For RGO with monovacancy,

$$E'_N = \Delta'\mu = E'_{RGO/FeCo} - E'_{RGO} - E_{FeCo} \qquad (3)$$

And for RGO with divacancy,

$$E''_N = \Delta''\mu = E''_{RGO/FeCo} - E''_{RGO} - E_{FeCo}$$

The $E'_N$ ($\Delta'\mu$), $E''_N$ ($\Delta''\mu$), $E'_{RGO/FeCo}$, $E''_{RGO/FeCo}$, $E'_{RGO}$, $E''_{RGO/FeCo}$ and $E_{FeCo}$ are the nucleation energy (chemical potential) of the reaction (3) and (4), system energy of RGO with monovacancy and magnetic particle FeCo, system energy of RGO with divacancy (5–8–5 defect) and magnetic particle FeCo, energy of monovacancy-RGO, divacancy-RGO and FeCo particle. Because the studied system involved in condensed phases, we assume that the entropy Δ(TS) and D(PV) terms have negligible contribution to the chemical potential [29]. According to the calculated result shown in Table.2, the divacancy has a more negative value of Δμ. Because a more negative value of E$_N$ indicates a more thermodynamically favorable process, the FeCo magnetic particles were easier to nucleate and grow up to cubic nano particles at larger defect locations (Fig. 8g–i) [28], which means that the distribution and size of FeCo aggregates positively correlated with the distribution and size of the defects. Therefore, the morphology of the FeCo magnetic particles could be used to characterize the

**Table 1** The content of oxygen-containing functional groups in films after electro-reduction and thermal reduction

| Methods | C–C/C=C (%) | C–O (%) | C=O | COOH |
|---|---|---|---|---|
| 10A, 1 h | 88.26 | 11.74 | 0 | 0 |
| 1150 °C, 1 h | 83.28 | 12.54 | 3.58% | 0.60% |
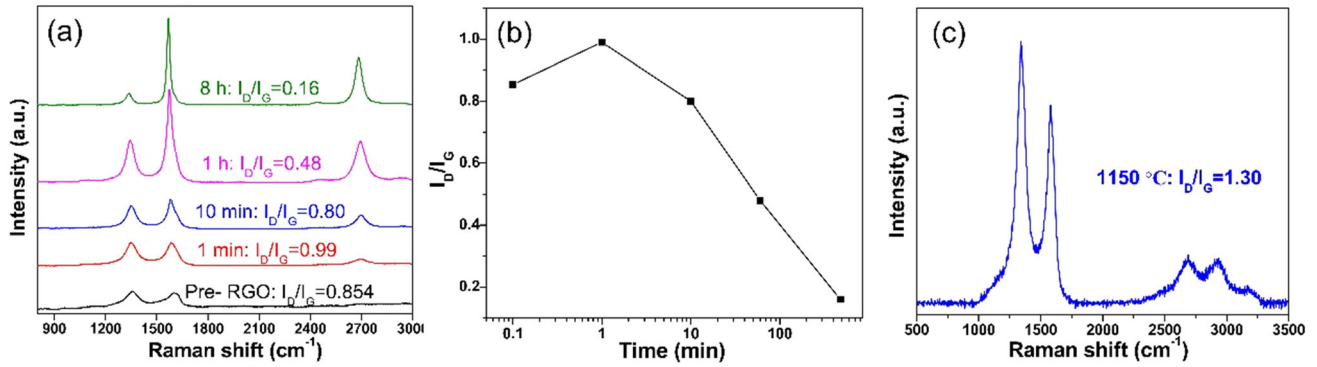
**Fig. 7** Raman results of RGO films. **a** Raman spectra of Pre-RGO and 10 A electro-reduced samples reduced for 1 min, 10 min, 1 h and 8 h. **b** Intensity ratio of D peak to G peak ($I_D/I_G$) of RGO films in (**a**). **c** Raman spectrum of thermal reduced film (1150 °C, 1 h). The temperature was set according to that of electro-reduction (10 A, 1 h)
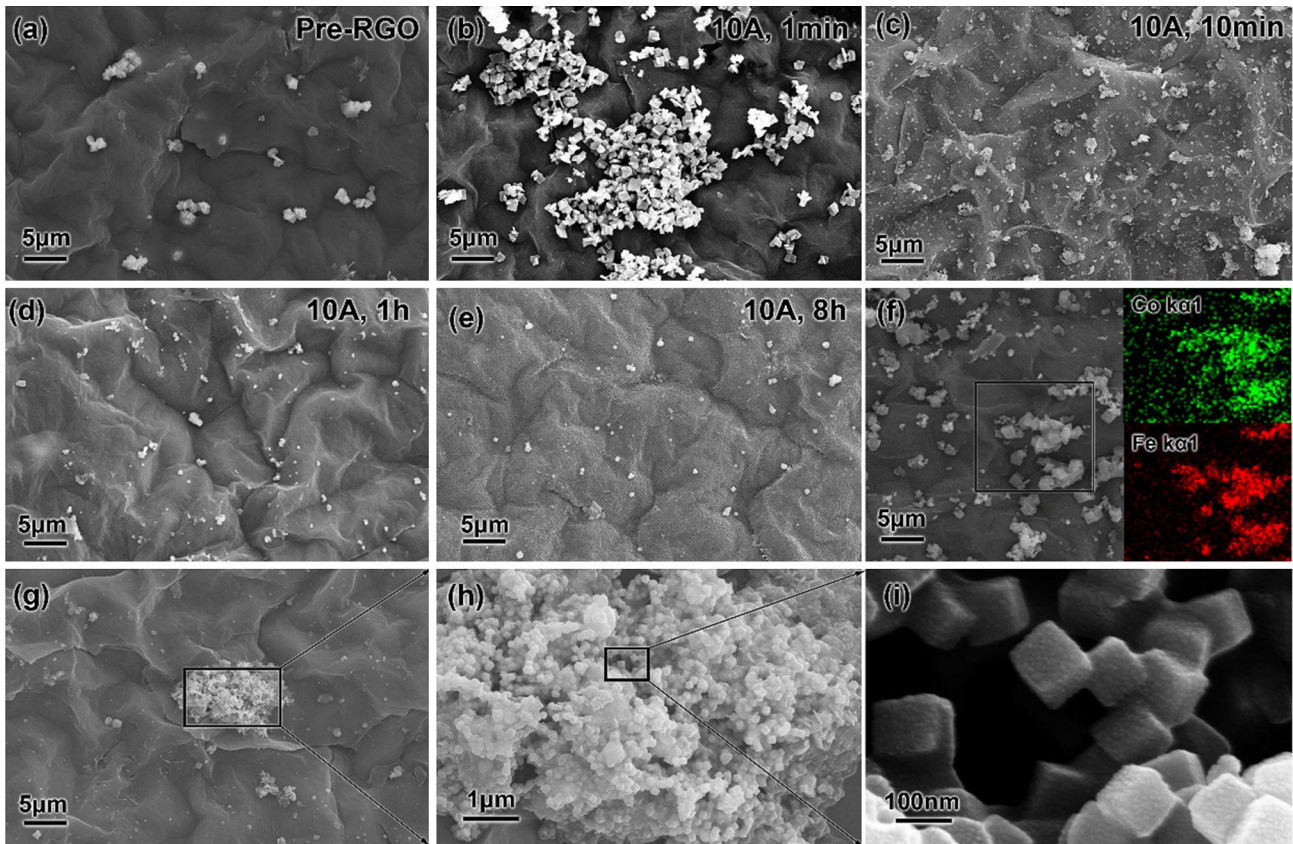


**Fig. 8** SEM images of **a** Pre-RGO (0 min), **b** 1 min, **c** 10 min, **d** 1 h and **e** 8 h electro-reduced samples at 10A after loading magnetic particles; **f** EDS image of element map; Morphology of FeCo particles at the magnifications of **g** ×2000, **h** ×10,000 and **i** ×100,000

defects on the RGO films. The results are consistence with the results of Raman spectrum.

The reduction of graphene oxide includes the removal of oxygen-containing functional groups and the repair of the sp$^2$ structure. The removal of oxygen-containing functional groups usually leads to the increase of defects, including vacancies left after the removal of oxygen-containing function groups and defects caused by the escape of gas ($H_2O$, $CO$, $CO_2$) generated during reduction [30–33], while the repair of the sp$^2$ structure led to the decrease of defects. During the electro-reduction process, the removal of

**Fig. 9** Optimized structures of FeCo on RGO with monovacancy (right) and divacancy (left)



divacancy　　　　　　　　　　　monovacancy
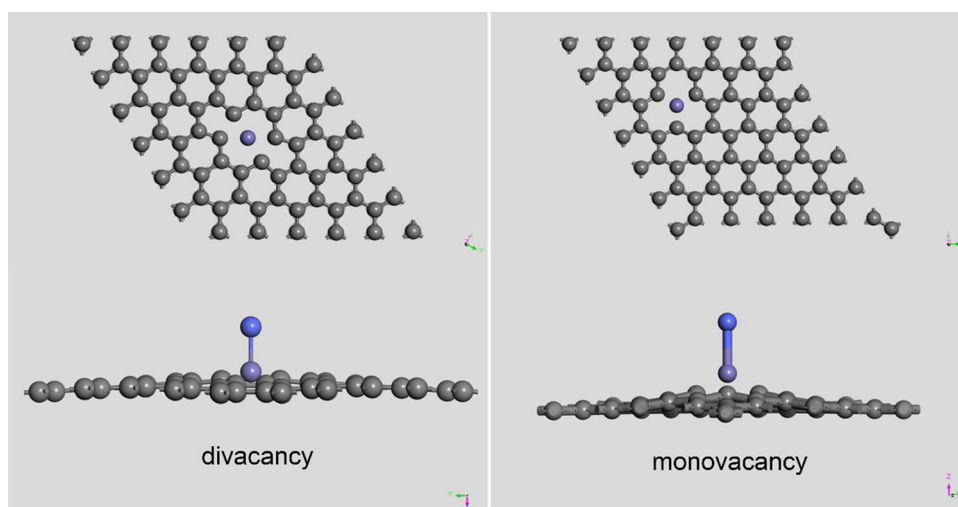
**Table 2** DFT calculated energies of monovacancy and divacancy system

| Energy (eV) | Divacancy | Monovacancy |
|---|---|---|
| $E_{RGO}$ | − 11,030.61 | − 11,192.57 |
| $E_{FeCo}$ | − 1946.59 | − 1946.59 |
| $E_{RGO/FeCo}$ | − 12,995.85 | − 13,154.32 |
| $\Delta\mu(E_N)$ | − 18.64 | − 15.15 |

oxygen-containing functional groups dominated in the first stage, which caused the defects in the RGO films increase, as shown in Fig. 8b. The increase of $I_D/I_G$ in the Raman spectrum also certified the increase of defects in the RGO films. As the reduction time increased, the removal of oxygen-containing functional groups become slower, the repair of the $sp^2$ structure dominated, which leads the defects in the RGO film gradually decreased, as shown in Fig. 8c and d. The $I_D/I_G$ in the Raman spectrum also decreased. Compared with the thermal reduction, both the removal of oxygen-containing functional groups and the repair of the $sp^2$ structure were accelerated by current. The $I_D/I_G$ of the RGO film reduced at 1150 °C for 1 h is 1.30 (Fig. 7c), which is still higher than that of Pre-RGO film, while the RGO film electro-reduced at 10 A for 10 min or 1 h is already lower than that of Pre-RGO film, which means the removal of oxygen-containing functional groups is much faster under electric current. After electro-reduction at 10 A for 8 h, the $I_D/I_G$ reaches 0.16, indicating a successful reduction of the RGO film. Therefore, the electro-reduction method may

provide new possibilities for fabricating high-quality graphene films in an energy-efficient and low-cost manner.

The electrical conductivity of the electro-reduced film is shown in Fig. 10. It is clear that the electricity conductivity increases with the reduction time (Fig. 10a). After electro-reduction at 10 A for 1 h, the conductivity of the film reaches 1140 S/cm, while the conductivity of the RGO film reduced at 1150 °C for 1 h was only 563 S/cm. After electro-reduction at 10 A for 8 h, the electrical conductivity of the film can reach 1840 S/cm. This result is better than the electrical conductivity of most RGO films reduced below 2000 K (Fig. 10b and Table. 3). [14, 23, 24, 34–45]

## 4 Conclusion

A method of reducing graphene oxide film under dc electrical current was reported. In this electro-reduction RGO film, the ratio of C/O reach as high as 132.33, and the conductivity is 1840 S/cm. The electro-reduction process includes two stages: removal of oxygen-containing functional groups and the repair of the $sp^2$ structure, both of which were accelerated by electrical current. Therefore, electro-reduction can achieve a better reduction effect in a lower temperature and a shorter time, which makes it an effective way to reduce GO film.
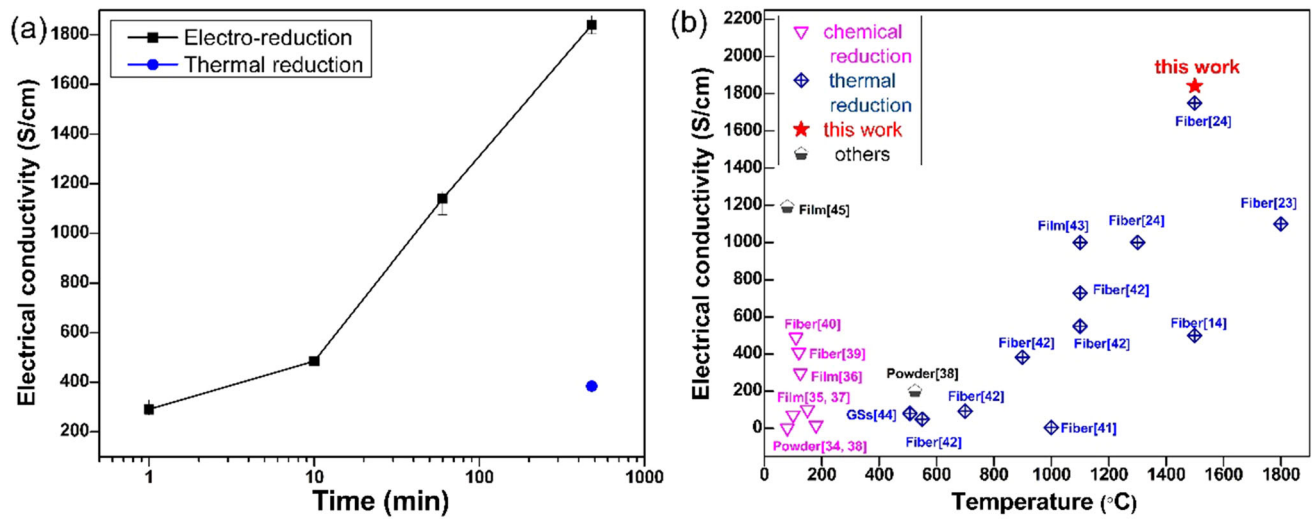
**Fig. 10** **a** Conductivity of the thermal reduced sample and electro-reduced samples reduced for 1 min, 10 min, 1 h and 8 h at 10 A. **b** The dc conductivity of RGO reported by other literatures [14, 23, 24, 34–45].

**Table 3** Comparison of dc conductivity σ by different methods

| Ref. no | Reduction method | | σ(S/cm) |
|---|---|---|---|
| [34, 35, 37] | | Hydrazine/Hydrazine hydrate/Hydrazine monohydrate | 2–99.6 |
| [38] | Chemical | $NaBH_4$ solution/$NaBH_4$ solution + Concentrated $H_2SO_4$ | 0.8–16.6 |
| [37, 39] | | 55% HI reduction/Vitamin C/wet drawing | 202–410 |
| [14, 23, 24, 41–44] | Thermal | $T \leq 2000$ °C | 5–1750 |
| [38, 45] | Others | Long-chainπbridging/Argon arc discharge | 202–1192 |
| – | This work | electric field + low temperature[a] | 1840 |

[a]This work mainly studies the electro-reduction with low temperature (< 1500 °C), other works by this method with high temperature(≥ 2000 K) did not show up in this table

# Acknowledgements

**Compliance with ethical standards**

**Conflict of interest** On behalf of all authors, the corresponding author states that there is no conflict of interest.

**Supplementary Information:** The online version contains supplementary material available at http s://doi.org/10.1007/s10854-021-05797-7.

# References

1. J. Hansson, C. Zandén, L. Ye, and J. Liu, 16th Int. Conf. Nanotechnol. - IEEE NANO 2016, 371 (2016).
2. N. Burger, A. Laachachi, M. Ferriol, M. Lutz, V. Toniazzo, D. Ruch, Prog. Polym. Sci. **61**, 1 (2016)
3. A.L. Moore, L. Shi, Mater. Today. **17**, 163–174 (2014)
4. K.S. Novoselov, A.K. Geim, S.V. Morozov, D. Jiang, Y. Zhang, S.V. Dubonos, I.V. Grigorieva, A.A. Firsov, Science **306**(5696), 666–669 (2004)
5. R.R. Nair, H.A. Wu, P.N. Jayaram, I.V. Grigorieva, A.K. Geim, Science **335**, 442–444 (2012)
6. A.K. Geim, K.S. Novoselov, Nat. Mater. **6**, 183–191 (2007)
7. M.S. Yazici, D. Krassowski, J. Prakash, J. Power Sources **141**(1), 171–176 (2005)
8. S. Pei, H.M. Cheng, Carbon N. Y. **50**, 3210–3228 (2012)
9. L.G. Guex, B. Sacchi, K.F. Peuvot, R.L. Andersson, A.M. Pourrahimi, V. Ström, S. Farris, R.T. Olsson, Nanoscale **9**, 9562–9571 (2017)

10. Y. Wang, Y. Chen, S.D. Lacey, L. Xu, H. Xie, T. Li, V.A. Danner, L. Hu, Mater. Today. **21**, 186–192 (2018)

11. Y. Chen, Y. Wang, S. Zhu, K. Fu, X. Han, Y. Wang, B. Zhao, T. Li, B. Liu, Y. Li, J. Dai, H. Xie, T. Li, J.W. Connell, Y. Lin, L. Hu, Mater. Today. **24**, 26–32 (2019)

12. Y. Chen, K. Fu, S. Zhu, W. Luo, Y. Wang, Y. Li, E. Hitz, Y. Yao, J. Dai, J. Wan, V.A. Danner, T. Li, L. Hu, Nano Lett. **16**, 3616–3623 (2016)

13. Y. Liu, C. Liang, A. Wei, Y. Jiang, Q. Tian, Y. Wu, Z. Xu, Y. Li, F. Guo, Q. Yang, W. Gao, H. Wang, C. Gao, Mater. Today NANO **3**, 1 (2018)

14. S.H. Noh, W. Eom, W.J. Lee, H. Park, S.B. Ambade, S.O. Kim, T.H. Han, Carbon N. Y. **142**, 230–237 (2019)

15. X. Huang, X. Zhang, J. Alloys Compd. **805**, 26 (2019)

16. X. Liu, W. Lu, X. Zhang, Acta Mater. **183**, 51 (2020)

17. T. Osada, N. Nagashima, Y. Gu, Y. Yuan, T. Yokokawa, H. Harada, Scr. Mater. **64**, 892 (2011)

18. X.L. Wang, J.D. Guo, Y.M. Wang, X.Y. Wu, B.Q. Wang, Appl. Phys. Lett. **89**, 61910 (2006)

19. D.C. Marcano, D.V. Kosynkin, J.M. Berlin, A. Sinitskii, Z. Sun, A. Slesarev, L.B. Alemany, W. Lu, J.M. Tour, ACS Nano **4**, 4806 (2010)

20. Q. Wei, S. Pei, X. Qian, H.M. Cheng, W. Ren, Adv. Mater. **32**, 1 (2020)

21. J. Zhong, W. Sun, Q. Wei, X. Qian, H.M. Cheng, W. Ren, Nat. Commun. **9**, 1 (2018)

22. W. Dai, L. Lv, J. Lu, ACS Nano **13**, 1547 (2019)

23. G. Xin, T. Yao, H. Sun, S.M. Scott, D. Shao, G. Wang, J. Lian, Science **349**, 1083–1087 (2015)

24. Z. Xu, Y. Liu, X. Zhao, L. Peng, H. Sun, Y. Xu, X. Ren, C. Jin, P. Xu, M. Wang, C. Gao, Adv. Mater. **28**, 6449 (2016)

25. V. Loryuenyong, A. Buasri, Adv. Mater. Sci. Eng. 2013 (2013).

26. R. Saito, M. Hofmann, G. Dresselhaus, A. Jorio, M.S. Dresselhaus, Adv. Phys. **60**, 413–550 (2011)

27. A.C. Ferrari, D.M. Basko, Nat. Nanotechnol. **8**, 235–246 (2013)

28. J. Yuan, C. Li, Z. Liu, D. Wu, L. Cao, CrystEngComm **19**, 6506–6515 (2017)

29. X. Li, W. Qi, D. Mei, M.L. Sushko, I. Aksay, J. Liu, Adv. Mater. **24**, 5136–5141 (2012)

30. Y. Huang, Q. Gong, Q. Zhang, Y. Shao, J. Wang, Y. Jiang, M. Zhao, D. Zhuang, J. Liang, Nanoscale **9**, 2340–2347 (2017)

31. S. Eigler, C. Dotzer, A. Hirsch, M. Enzelberger, P. Mu, Chem. Mater. **24**(7), 1276–1282 (2012)

32. J. Rodríguez-Mirasol, T. Cordero, J.J. Rodríguez, Carbon **34**(1), 43–52 (1996)

33. H. Pan, X. Ren, H. Yuan, Mater. Rev. **28**(6), 93–96 (2014)

34. S. Stankovich, D.A. Dikin, R.D. Piner, K.A. Kohlhaas, A. Kleinhammes, Y. Jia, Y. Wu, Carbon **45**(7), 1558–1565 (2007)

35. D. Li, M.B. Müller, S. Gilje, R.B. Kaner, G.G. Wallace, Nat. Nanotechnol. **3**(2), 101–105 (2008)

36. S. Pei, J. Zhao, J. Du, W. Ren, H. Cheng, Carbon N. Y. **48**, 4466 (2010)

37. M.J. Fernandez-Merino, L. Guardia, J.I. Paredes, J. Phys. Chem. C. **114**, 6426–6432 (2010)

38. W. Gao, L.B. Alemany, L. Ci, P.M. Ajayan, Nat. Chem. **1**, 403 (2009)

39. Z. Xu, H. Sun, X. Zhao, C. Gao, Adv. Mater. **25**(2), 188–193 (2013)

40. Z. Xu, Y. Zhang, P. Li, C. Gao, ACS Nano **6**(8), 7103–7113 (2012)

41. Z. Li, C. Gao, Nat. Commun. **7**, 1 (2016)

42. X. Wang, L. Zhi, K. Mu, Nano Lett. **8**(1), 323–327 (2008)

43. H.A. Becerril, J. Mao, Z. Liu, ACS Nano **2**(3), 463–470 (2008)

44. Z. Wu, W. Ren, L. Gao, J. Zhao, Z. Chen, B. Liu, D. Tang, B. Yu, C. Jiang, H. Cheng, ACS Nano **3**(2), 411–417 (2009)

45. S. Wan, Y. Chen, A.P. Tomsia, S. Wan, Y. Chen, Y. Wang, G. Li, G. Wang, L. Liu, J. Zhang, Matter **1**, 389–401 (2019)